LAWRENCE
LIVERMORE
NATIONAL
LABORATORY

LLNL-PROC-816409

A new toroidal x-ray crystal spectrometer for the diagnosis of high energy density plasmas at the National Ignition Facility

M. Bitter, K. W. HIill, L. Gao, B. F. Krauss, P. C. Efthimion, L. Delgado-Aparicio, N. Pablant, B. Stratton, M. Schneider, F. Coppari, R. Kauffman, A. G. MacPhee, Y. Ping, D. Thorn

November 4, 2020

22nd Topical Confer- ence on High-Temperature Plasma Diagnostics
San Diego, CA, United States
April 16, 2018 through April 19, 2018

Disclaimer

A new toroidal x-ray crystal spectrometer for the diagnosis of high energy density plasmas at the National Ignition Facility

M. Bitter,[1,a)] K. W. Hill,[1] Lan Gao,[1] B. F. Kraus,[1] P. C. Efthimion,[1] L. Delgado-Aparicio,[1] N. Pablant,[1] B. Stratton,[1] M. Schneider,[2] F. Coppari,[2] R. Kauffman,[2] A. G. MacPhee,[2] Y. Ping,[2] and D. Thorn[2]
[1]*Princeton Plasma Physics Laboratory, Princeton, New Jersey 08543, USA*
[2]*Lawrence Livermore National Laboratory, Livermore, California 94550, USA*

The here-described spectrometer was developed for the extended x-ray absorption fine structure spectroscopy of high-density plasmas at the National Ignition Facility. It employs as the Bragg reflecting element a new type of toroidally bent crystal with a constant and very large major radius R and a much smaller, locally varying, minor radius r. The focusing properties of this crystal and the experimental arrangement of the source and detector make it possible to (a) fulfill the conditions for a perfect imaging of an ideal point source for each wavelength, (b) obtain a high photon throughput, (c) obtain a high spectral resolution by eliminating the effects of source-size broadening, and (d) obtain a one-dimensional spatial resolution with a high magnification perpendicular to the main dispersion plane. *Published by AIP Publishing.* https://doi.org/10.1063/1.5036806

I. INTRODUCTION

X-ray diffraction (XRD) and the Extended X-ray Absorption Fine Structure (EXAFS) spectroscopy are among the most widely used diagnostics in high pressure condensed matter studies because of their capability to provide information about the structural transformations occurring in the material at the atomic level. Developing these techniques to study samples that have been ramp-compressed to very high pressures will extend knowledge of matter at extreme conditions. These conditions can be achieved using large lasers to do the compression, such as the National Ignition Facility (NIF) lasers at the Lawrence Livermore National Laboratory or the OMEGA laser at the Laboratory for Laser Energetics (Rochester, NY).[1] A major challenge for the EXAFS spectroscopy at these facilities is, however, the development of a spectrometer, which satisfies the simultaneous requirements of a high spectral resolution and a high photon-throughput, for an extended spectral range. Notably, the effects of source-size broadening, which limit the spectral resolution, have been so troubling that, ultimately, in order to mitigate these effects, painstaking "source development" experiments were conducted at the NIF to reduce the source size itself.[1,2]

An important step toward a solution of the source-size broadening problem by an improved spectrometer design was made by Koch,[3] who proposed the use of a modified Johann spectrometer with a spherical Ge-220 crystal of a large radius of **R** = 4826 mm, where the x-ray source would be close to the crystal to enhance the photon-throughput and where the detector would be placed on the Rowland circle—see Fig. 1—to eliminate the effects of source-size broadening, since—at the Rowland circle—the separation of the rays, which emanate from different points of an extended source and which are Bragg reflected with the same Bragg angle **Θ**, is minimal.

Koch's spectrometer design had, however, two shortcomings:

1. The distance, d_{SC} = 150 mm, of the source from the central point on the crystal surface was much shorter than the crystal's sagittal focal length, which—for the main Bragg angle in Koch's design of $\theta_0 = 13.72°$—amounted to $f_s = \frac{R}{2\cdot\sin(\theta_0)} = 10\,174$ mm. The image of the source was therefore a virtual image, which was located behind the crystal, at the distance, d_{IM} = 152.24 mm, from the central point on the crystal's surface. The reflected rays, which seem to emanate from this virtual image, were therefore divergent, and their points of intersection with the detector plane were spread out on an elliptical arc of

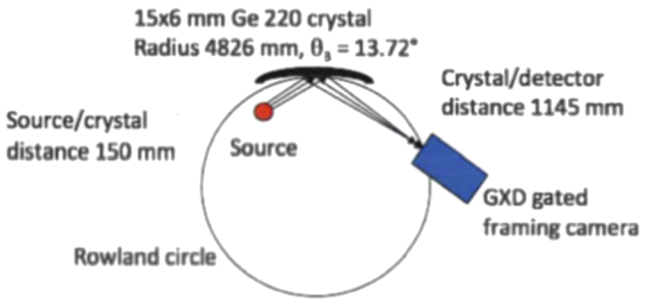

FIG. 1. Original figure from Koch's proposal.[3]—We point out that the parameter values used in Fig. 1 differ from those which are quoted. The Bragg angle, source-crystal distance, and crystal-detector distance shown are 35° (instead of 13.72°), 1380 mm (instead of 150 mm), and 2768 mm (instead of 1145 mm), respectively.

Note: Paper published as part of the Proceedings of the 22nd Topical Conference on High-Temperature Plasma Diagnostics, San Diego, California, April 2018.
a)Author to whom correspondence should be addressed: bitter@pppl.gov

the length **H**, which was determined by the height **h** of the crystal,

$$H = \frac{d_{IM} + R \cdot \sin(\theta_0)}{d_{IM}} \cdot h = 8.5 \cdot h,$$

so that for a modest height of the crystal of $h = 10$ mm, the height of the detector needed to be $H = 85$ mm in order to collect all the reflected photons. The useful height of the crystal and hence the attainable photon throughput were thus ultimately limited by the height **H** of the detector. It is not possible to increase the photon throughput beyond this limit by moving the source still closer to the crystal since the reflected rays are then even more divergent—the realization of Koch's idea of increasing the photon throughput by moving the source close to the crystal is, therefore, actually very much constrained.

2. Koch's other suggestion, namely, to eliminate the source-size broadening effects by placing the detector on the Rowland circle, is not specific enough, and for his chosen orientation of the detector plane—perpendicular to the main reflected ray for the Bragg angle $\theta_0 = 13.72°$—the source-size broadening effects are only eliminated for the wavelength, which is associated with the Bragg angle θ_0 but not for the entire spectral range.

Our new spectrometer design, which is described in Sec. II, eliminates these shortcomings of Koch's design and satisfies the imaging conditions for each wavelength perfectly. Also, the effects of source-size and crystal-thickness broadening are eliminated for the entire spectral range of interest by positioning the detector at the tangency point of the proper tangency circle (see Sec. II) for each wavelength. Thus, it is possible to obtain at once a high photon throughput, a high spectral resolution, and a one-dimensional spatial resolution perpendicular to the main dispersion plane with a high magnification.

II. A NEW EXAFS SPECTROMETER

A. Spectrometer design

Figure 2 shows the ray pattern for Koch's design in more detail and introduces the concept of the "tangency circle,"

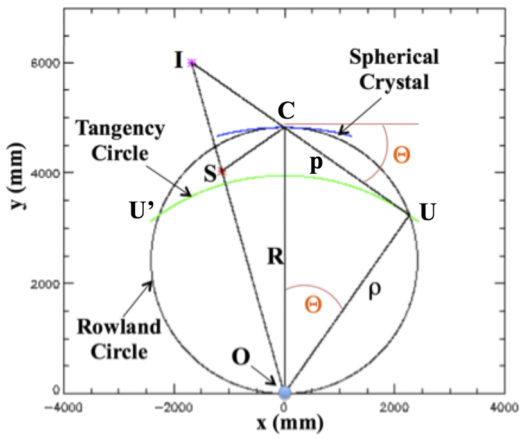

FIG. 2. More detailed ray pattern for Koch's design, using the actual dimensions of Fig. 1.

which is used for our new design. The point **O** is the center of the crystal sphere and a center of symmetry since any straight line through **O** is an axis of the rotational symmetry that can be used for imaging. Since the imaging conditions require that the point source **S** and its image point **I** are fixed points with respect to a rotation of the ray pattern, these points must be on an axis of rotation, which—in the case of a sphere—must also pass through **O**. This axis of the rotational symmetry is therefore uniquely defined if the position of the source **S** is given. The image **I** is then at the point of intersection of the axis of rotation with the reflected ray. For Koch's design, the image **I** is a virtual image, which is located behind the crystal, see Fig. 2. By rotating the ray pattern in Fig. 2 about the axis **OSI**, one can easily visualize that the reflected rays describe a cone with the apex at **I**. The reflected rays are, therefore, divergent and their points of intersection with a detector plane, which is oriented along **OU** and perpendicular to the main dispersion plane, describe a conic section, which is often an ellipse.

We also infer from Fig. 2 that the reflected ray in the main dispersion plane is—at its intersection point **U** with the Rowland circle—tangential to the circle with the radius $\rho = R\cos(\theta)$ about **O** since the distance of **CU** is equal to $p = R\sin(\theta)$ and since the Rowland circle is the Thales circle. The points **U′** and **U**, which are usually described as the intersection points of the incident and reflected rays with the Rowland circle, can therefore also be defined as the tangency points of the incident and reflected rays on the sphere with the radius $\rho = R\cos(\theta)$ about **O**; the green circle in Fig. 2 is then the trace of this sphere in the main dispersion plane. The definitions of the Rowland circle and the tangency sphere are substantially different: The tangency sphere maintains the spherical symmetry of the ray pattern since it is concentric with the crystal sphere. It can therefore conveniently be used to describe the incident and reflected rays at each crystal point, for a given Bragg angle **Θ**. By contrast, the definition of the Rowland circle breaks the spherical symmetry by singling out a particular crystal point, e.g., the point **C** in Fig. 2, since the Rowland circle passes through **O** and a particular point of Bragg reflection. In principle, one must define a Rowland circle for each crystal point so that there are an infinite number of equivalent Rowland circles.

The concept of the "tangency" sphere is also useful for a description of the ray pattern from an extended source, a derivation of the Johann error and an understanding of the source-size broadening effects. For this purpose, we consider in Fig. 3 the ray pattern from an extended source for the Bragg angle **Θ** = 59° > 45°, where the images **I** are real. The ray pattern, shown in Fig. 3, is actually a superposition of the identical ray patterns from three source points $\mathbf{S}_0$, $\mathbf{S}_1$, and $\mathbf{S}_2$ of an extended source. The points $\mathbf{C}_0$, $\mathbf{C}_1$, and $\mathbf{C}_2$ and $\mathbf{U}_0$, $\mathbf{U}_1$, and $\mathbf{U}_2$ are, respectively, the points of Bragg reflection and the tangency points for the reflected rays on the tangency circle with $\rho = R\cos(\theta)$. The points $\mathbf{U}_0$, $\mathbf{U}_1$, and $\mathbf{U}_2$ are also the positions of the real images $\mathbf{I}_0$, $\mathbf{I}_1$, and $\mathbf{I}_2$. Since the three ray patterns are identical, they can be made congruent by a rotation about an axis through **O** that is perpendicular to the drawing plane of Fig. 3 by an angle **α**. We infer from Fig. 3 that the reflected rays from $\mathbf{C}_1$ (red ray) and $\mathbf{C}_2$ (green ray) intersect each other at a point outside of and at a distance **ξ** from

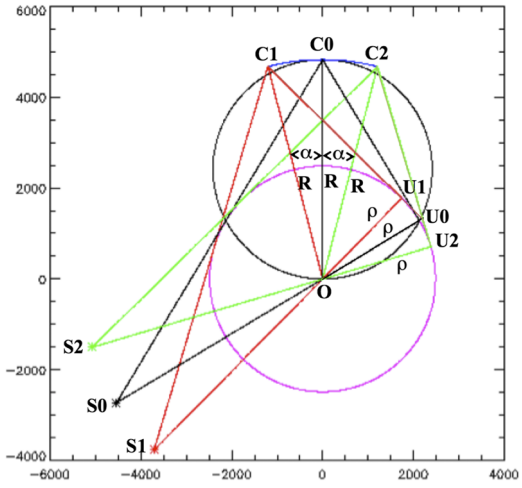

FIG. 3. Ray pattern for the Bragg angle Θ = 59° and three source points $\mathbf{S}_0$, $\mathbf{S}_1$, and $\mathbf{S}_2$ of an extended source.

the tangency circle on the extension of the line segment $\mathbf{OU}_0$. This distance ξ is given by the equation $(\rho + \xi)\cos(\alpha) = \rho$, and the solution of this equation, if **ξ** and **α** can be considered as small quantities, is the well-known Johann error, $\xi = \rho\frac{\alpha^2}{2} = \frac{w^2}{8R}\cos(\theta)$, where **α** has been expressed by the width $\mathbf{w} = \mathbf{C}_1\mathbf{C}_2$ of the crystal.

The Johann error is the minimum separation between the rays, which emanate from an extended source and which are Bragg reflected from a spherical crystal of the width **w** with the Bragg angle **Θ**. This minimum occurs at the tangency point $\mathbf{U}_0$, which is therefore the preferred detector position, if it is necessary to eliminate source-size broadening effects in order to enhance the spectral resolution. Evidently, the spatial extension of a source will not be noticeable if the detector is placed at $\mathbf{U}_0$ and if the Johann error is smaller than the detector resolution.

Also the detrimental effects to the spectral resolution which result from the penetration of the x-rays to lattice planes deep inside the crystal, the so-called crystal-thickness broadening, can be minimized by positioning the detector at $\mathbf{U}_0$, since the Bragg reflection from those lattice planes leads to a lateral displacement of the exiting (Bragg reflected) ray from the incident ray on the front surface of the crystal that is similar to the displacement between the Bragg reflection points ($\mathbf{C}_1$ and $\mathbf{C}_2$ in Fig. 3) in the case of an extended source. The crystal-thickness broadening leads thus to an additional Johann error at $\mathbf{U}_0$ that could be subsumed in the Johann error, which results from the spatial extension of the source.

In the following, we describe our design of an EXAFS spectrometer for the x-ray energies $8.877 \le E \le 10.877$ keV which include the energy of the TaL_3 absorption edge at 9.877 keV. Our design is based on Koch's original design. But instead of a spherical crystal, we use a toroidally bent crystal with a varying minor radius. This special crystal shape evolved from an application of basic physics principles as we tried to satisfy the imaging conditions for each wavelength and to generate a real image at the tangency point of the reflected rays with the proper tangency spheres. The essential features of our design are shown in Fig. 4 and are further explained below.

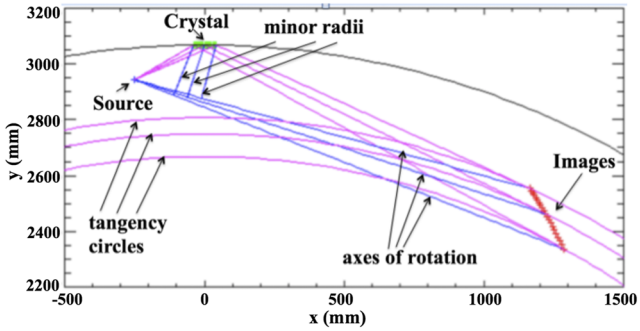

FIG. 4. Arrangement of source, crystal, and image points in the main dispersion plane (x, y-plane).

The crystal is a Ge[400]-crystal with the 2d-lattice spacing of $2d = 2.828\,68$ Å and a large major radius $\mathbf{R} = 3068$ mm. Its trace in the main dispersion plane is shown by the black circle with the radius **R** about the point (x = 0; y = 0). Also, similar to Koch's design, the source is placed at a short distance, d_{SC} = 280 mm, from the central point (x = 0; y = R) on the crystal surface. The points, shown in green, represent 21 crystal points, which are the points of Bragg reflection for 21 equidistant x-ray energies in the interval from 8.877 to 10.877 keV. The central crystal point at x = 0, y = **R** is associated with the energy E = 9.877 keV of the TaL_3 absorption edge. The points, shown in red, are the tangency points of the Bragg reflected rays in the main dispersion plane with the circles of the radii $\rho = R{\cdot}\cos(\theta)$ about x = 0, y = 0 for those 21 x-ray energies. Only three of these tangency circles, for the energies E = 8.877; 9.877; 10.877 keV and the corresponding Bragg angles Θ = 29.588°; 26.345°; 24.482°, are shown in magenta in Fig. 4 together with the incident and reflected rays. In order to create, for each wavelength, a real image of the source at the tangency point for the Bragg reflected ray with the proper tangency circle in the main dispersion plane, we demand that the interconnecting straight (blue) lines between the source and the tangency point for each wavelength are the axes of the rotational symmetry for the crystal. The source point and the tangency points are then fixed points with respect to the rotations of the ray patterns for each wavelength about those axes. The short line segments (*blue*), which are normal to these axes of the rotational symmetry and which extend from these axes up to the points of Bragg reflection, represent the locally varying minor radii **r** of a toroidally bent crystal. We point out that according to the above given formula, the Johann error at the here-defined image points would only be about 0.3 μm for a relatively large, 2 mm wide, extended source and our design parameters.

B. Dispersion

The wavelength dispersion is defined as $\frac{d\lambda}{ds}$, where λ is the wavelength and s is the length of the arc on which the image points are distributed in the main dispersion plane. We use the following formula:

$$\frac{ds}{d\lambda} = \sqrt{\left(1 + \frac{dy_I}{dx_I}\right)^2} \cdot \frac{dx_I}{d\lambda}. \qquad (1)$$

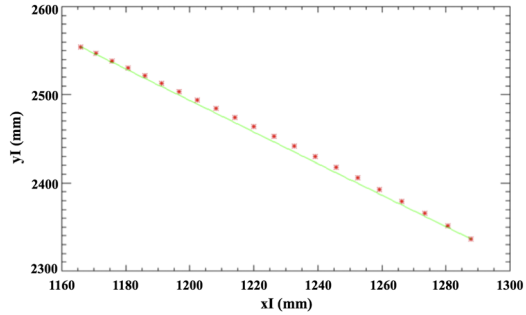

FIG. 5. Image points in the detector plane (*red*) and the straight line (*green*) connecting the end points (x_I = 1165.93 mm, y_I = 2554.36 mm) and (x_I = 1287.86 mm, y_I = 2336.51 mm).

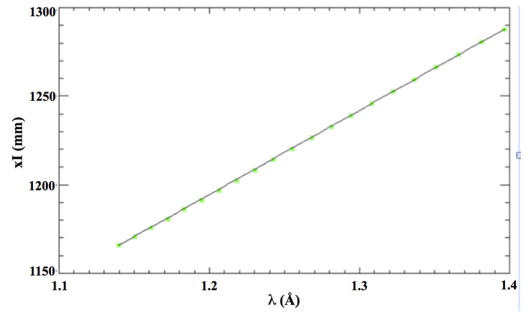

FIG. 6. Abscissa x_I of image points (*green*) as a function of λ and straight line (*blue*) connecting the endpoints.

where x_I and y_I are the coordinates of the image points in the main dispersion plane.

Figures 5 and 6 show the functions $y_i(x_I)$ and $x_i(\lambda)$ on enlarged scales and demonstrate that, for the parameters of our present design, these functions are well approximated by straight lines with the slopes $\frac{dy_I}{dx_I} = -1.79$ and $\frac{dx_I}{d\lambda} = 474.77$ (mm/Å). Inserting these numerical values in Eq. (1), we get

$$\frac{ds}{d\lambda} = 972.12\ (\text{mm/Å}) \qquad (1')$$

and

$$\frac{d\lambda}{ds} = 1.03\ (\text{mÅ/mm}). \qquad (2)$$

The resolving power derived from Eq. (2) for the case that the detector is an image plate, assuming a 100 μm detector resolution, is 12 000, which should be sufficient to accurately measure the EXAFS oscillations near the TaL_3 absorption edge since the period of these oscillations is about 50 eV—see Fig. 5(c) in Ref. 5 and Fig. 9(b) in Ref. 6.

The required length of the detector to cover the energy range, 8.877 < E < 10.877 keV, is

$$s = \frac{ds}{d\lambda} \cdot (\lambda_1 - \lambda_2) = 249.7\ \text{mm}, \qquad (3)$$

where λ_1 = 1.39 669 Å and λ_2 = 1.13 987 Å correspond to the x-ray energies of 8.877 and 10 877 keV.

C. Spatial resolution

Our spectrometer design also provides a 1D spatial resolution perpendicular to the main dispersion plane with a magnification $M = \frac{p}{q}$, where **p** and **q** are defined by

$$p + q = \sqrt{a^2 + b^2 + 2ab \cdot \cos(2\theta)} \qquad (4)$$

$$p - q = \frac{a^2 - b^2}{\sqrt{a^2 + b^2 + 2ab \cdot \cos(2\theta)}} \qquad (5)$$

with $a = R \cdot \sin(\theta)$ and $b = d_{SC}(\theta)$, the distance of the source from the point of Bragg reflection on the crystal for the Bragg angle **Θ**. For our design parameters and $\theta = 26.345°$, $M = 6.737$.

III. DISCUSSION AND CONCLUSIONS

The novelty of our spectrometer is a toroidally bent crystal with a varying minor radius, which changes in magnitude and direction along the crystal surface to establish, at each crystal point, the proper rotational symmetry for the imaging of an ideal point source. The axis of the rotational symmetry and the minor radius are at each crystal point uniquely defined by the law of Bragg reflection and the positions of the source and image on the incident and reflected rays. In particular, one can choose a source position close to the crystal to enhance the photon throughput and then generate, for each wavelength, a real image at the point with the minimum Johann aberration in order to eliminate the effects of source-size broadening. In doing so, one obtains not only a high spectral resolution but also a high spatial resolution perpendicular to the main dispersion plane. We point out that, in Koch's design, the divergence of the reflected rays precludes the possibility of obtaining a spatial resolution. Our new toroidal crystal spectrometer offers, therefore, a high degree of flexibility and new features that are unmatched by any of the existing spectrometers. In fact, the toroidal crystal spectrometers, which are presently being used for the diagnosis of laser-produced plasmas—see, e.g., Gamoa *et al.*[4]—are distinctly different from our spectrometer due to the fact that these spectrometers use a conventional toroidal crystal form with a constant minor radius which at every crystal point is aligned normal to the crystal surface.

The differences between our spectrometer and the traditional toroidal crystal spectrometer are further explained with the aid of Fig. 7, where the *black* circles with the radii **R** = 400 mm about **O** and $\mathbf{R_R}$ = **R**/2 about **M** represent the trace of a toroidal crystal and the Rowland circle in the main dispersion plane.[5] The crystal point **C** is the point of Bragg reflection. The ray, which is incident on **C** with the Bragg angle **Θ**, is assumed to emanate from an ideal point source that may be positioned at $\mathbf{S}_1$ or $\mathbf{S}_2$. We demand that the image of $\mathbf{S}_1$ or $\mathbf{S}_2$ is a real image at the point **I** on the Rowland circle.

In the case of a conventional torus, the major and minor radii, $\mathbf{R_t}$ and $\mathbf{r_t}$, are perfectly aligned with each other in the main dispersion plane. The axis, associated with the rotational symmetry of the ray pattern, must therefore be perpendicular to the straight line from **O** to **C** and pass through **I** and $\mathbf{S}_1$ since the source and image points must be on the axis of rotation. It

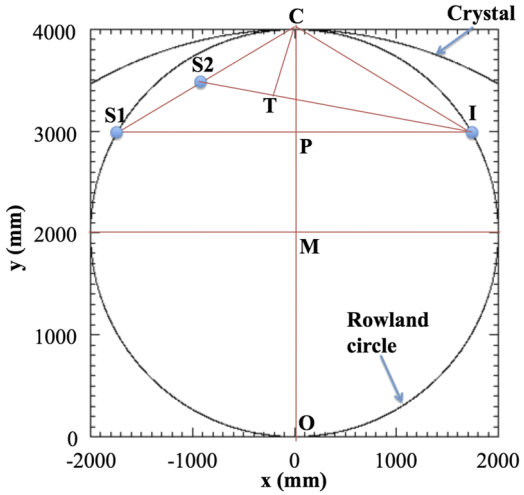

FIG. 7. Illustration of the differences between a torus with a varying minor radius and a conventional torus.

then follows that **I** and $\mathbf{S}_1$ both have to be on the Rowland circle, and the major and minor radii must be equal to $\mathbf{R_t} = \mathbf{OP}$ and $r_t = CP = R \cdot \sin^2(\theta)$ since the distances of $\mathbf{S}_1$ and **I**, from the point of Bragg reflection **C**, are equal to $R \cdot \sin(\theta)$. With a conventional toroidal crystal, one can simultaneously satisfy the conditions for imaging and eliminate the effects of source-size broadening for only one particular wavelength λ. The associated Bragg angle, Θ(λ), and minor radius, $\mathbf{r_t}(\boldsymbol{\lambda})$, must fulfill the relation $r_t = R\sin^2(\theta(\lambda))$. For this particular wavelength λ, one also obtains a 1D spatial resolution perpendicular to the main dispersion plane with the magnification of $\mathbf{M} = 1$. However, for any other wavelength and any other source and detector position, the basic physics principles for imaging are violated.

On the other hand, it is possible to construct, for any given image point **I** and source point $\mathbf{S}_2$, a torus with varying minor radius $r_t = CT = \sqrt{a^2 - p^2}$—see Fig. 7 and Sec. II C for an explanation of $\boldsymbol{a}$ and $\boldsymbol{p}$—such that the Bragg and imaging conditions are exactly fulfilled and, as we have shown in this paper, this can be done for each wavelength in an extended spectral range.

Our spectrometer design for EXAFS studies of the TaL_3 absorption edge will be tested at the Laboratory for Laser Energetics (LLE) in Rochester during this fall, and then, depending on the outcome of this test, it will also be used at the NIF. The specifications and procedures for the manufacture and alignment of a toroidal crystal with a varying minor radius are presently being defined and will be described in a subsequent paper.

ACKNOWLEDGMENTS

This work was performed under the auspices of the U.S. DoE by LLNL under Contract No. DE-AC52-07NA27344 and PPPL under Contract No. DE-AC02-09CH11466.

[1] F. Coppari, D. B. Thorn, G. E. Kemp, R. S. Craxton, E. M. Garcia, Y. Ping, J. H. Eggert, and M. B. Schneider, Rev. Sci. Instrum. **88**, 083907 (2017).
[2] A. Krygier, F. Coppari, G. E. Kemp, D. Thorn, R. S. Craxton, J. Eggert, E. M. Garcia, J. M. McNaney, H.-S. Park, Y. Ping, B. Remington, and M. Schneider, Rev. Sci. Instrum. **89**, 10F114 (2018).
[3] J. Koch, in LLNL X-ray Spectroscopy Workshop, 2015.
[4] E. J. Gamboa, C. M. Huntington, M. R. Trantham, P. A. Keiter, R. P. Drake, D. S. Montgomery, J. F. Benage, and S. A. Letzring, Rev. Sci. Instrum. **83**, 10E108 (2012).
[5] Y. Ping, D. G. Hicks, B. Yaakobi, F. Coppari, J. Eggert, and G. W. Collins, Rev. Sci. Instrum. **84**, 123105 (2013).
[6] Y. Ping and F. Coppari, High Pressure Res. **36**, 303 (2016).